

# **Record Performance of Electrical Injection Sub-wavelength Metallic-Cavity Semiconductor Lasers at Room Temperature**

K. Ding<sup>1</sup>, M. T. Hill<sup>2</sup>, Z.C. Liu<sup>1</sup>, L. J. Yin<sup>1</sup>, P. J. van Veldhoven<sup>2</sup>, and C.Z. Ning<sup>1\*</sup>

1: School of Electrical, Computer, and Energy Engineering, Arizona State University, Tempe, AZ 85287

2: COBRA Research Institute, Technische Universiteit Eindhoven, 5600 MB Eindhoven, The Netherlands

\* To whom all correspondence should be addressed: cning@asu.edu

**Metallic-Cavity lasers or plasmonic nanolasers of sub-wavelength sizes have attracted great attentions in recent years<sup>1-8</sup>, with the ultimate goal of achieving continuous wave (CW), room temperature (RT) operation under electrical injection. Despite great efforts, a conclusive and convincing demonstration of this goal has proven challenging. By overcoming several fabrication challenges imposed by the stringent requirement of such small scale devices, we were finally able to achieve this ultimate goal. Our metallic nanolaser with a cavity volume of  $0.67\lambda^3$  ( $\lambda=1591$  nm) shows a linewidth of 0.5 nm at RT, which corresponds to a Q-value of 3182 compared to 235 of the cavity Q, the highest Q under lasing condition for RT CW operation of any sub-wavelength laser. Such record performance provides convincing evidences of the feasibility of RT CW metallic nanolasers, thus opening a wide range of practical possibilities of novel nanophotonic devices based on metal-semiconductor structures.**

Truly nanoscale coherent light sources<sup>4</sup> with sub-wavelength<sup>9</sup> dimensions such as photonic crystal nanocavity lasers<sup>10-13</sup> are of great importance in both fundamental science and future technological applications. Plasmonic sub-wavelength scale lasers or spasers<sup>5</sup> represent the ultimate verification and utilization of the fundamental understanding of nanoscale physics processes involving the interactions of plasmons in metals or heavily doped semiconductors, excitons and electron-hole pairs in semiconductors, and photons confined in a cavity. Such nanolasers with sizes already comparable to modern day transistors will potentially lead to large scale integration of photonic and electronic functionalities, thus enabling unprecedented capabilities in a wide range of future technologies from computing and communication to sensing and detection. Recent years have witnessed a rapid progress in nanoscale lasers since the proposal of spasers<sup>5</sup> and of the semiconductor-metal core-shell laser architecture<sup>14</sup>, which was soon demonstrated with a top-down approach under electrical injection<sup>6</sup>. This paradigm shift in laser development represented by the use of metallic cavities operating in visible and near infrared wavelength ranges for reducing the device size down to the nanoscale, has since been further solidified with a myriad of designs and variations<sup>1-3, 7-8, 15-23</sup>. Many of the spasers or nanolasers, especially the recently demonstrated electrical injection plasmonic lasers with 90-nm wide semiconductor cores<sup>15</sup>, have characteristic dimensions already comparable to state-of-the-art transistors. Despite great success and various breakthroughs, the holy grail of this endeavor has remained out of reach, which is to achieve RT, CW operation of a truly nanoscale laser under electrical injection. While various aspects of this ultimate goal have been demonstrated, the simultaneous achievement of all these attributes would have far-reaching consequences. While optically and electrically pumped pulse operation at RT has been demonstrated, CW operation under electrical injection is fundamentally different due to exacerbated heat generation. This is

also true, even for other pure dielectric sub-wavelength lasers. Sub-wavelength microdisk lasers have been demonstrated at RT, but in pulse mode in visible<sup>24</sup> and near infrared<sup>18</sup> wavelength ranges. But CW operation<sup>25</sup> is still limited to low temperature under optical pumping. Therefore an unambiguous demonstration of RT CW operation of nanolaser with electrical injection represents a significant advance in the development of nanoscale lasers. While our recent work<sup>26,27</sup> has demonstrated CW operation under electrical injection with linewidth as broad as 3-4 nm, this progress itself raised new questions: Would such sub-wavelength lasers ever be able to show features of light output similar to a typical semiconductor laser with the expected narrow linewidth among others. This issue becomes especially important, since a few other reported nanolasers<sup>3,23</sup> showed even broader linewidth under RT CW operation and most of the proposed applications of nanolasers such as on chip sensing and communication require narrow linewidth<sup>28,29</sup>. Most importantly, the smooth and gradual transition near threshold in that demonstration also leads one to wonder: Is this smooth transition an intrinsic feature of such lasers due to large spontaneous emission factor associated with their small sizes and metallic cavities, or because of the non-ideal performance of a device incapable of operating far above threshold due to significant heating? All these questions are related to the fundamental features of such nanolasers and will ultimately determine the extent of all the potential applications of such lasers mentioned above.

In this paper, we intend to address all these questions by demonstrating a new generation of sub-wavelength lasers with record performance<sup>30</sup>. As we will show, sub-wavelength metallic-cavity lasers are capable of showing similar features of a typical laser, such as narrow linewidth and well-defined transition threshold, but with a cavity volume as small as  $0.67 \lambda^3$  ( $\lambda=1591$  nm). The

linewidth of our lasers is reduced by a factor of 13 from below to above threshold, with transition behavior similar to that of a typical semiconductor laser. To have a fair comparison of linewidth of lasers operating at different wavelengths, a relative linewidth,  $\Delta\lambda/\lambda$ , can be used, or better its inverse,  $\lambda/\Delta\lambda$ , which is the standard definition of Q factor for a signal. The concept of such Q-factor under lasing condition (or lasing  $Q^{31} = \lambda/\Delta\lambda$ ) is, identical to the total  $Q^{32}$  or observed  $Q^{33}$  including all losses and gain and a good measure of improvement of a laser mode above threshold from below threshold (cavity Q). Our Q-factor of 3182 under lasing condition is the highest reported value so far to our knowledge for RT CW nanolasers and comparable to or better than most pulse operation nanolasers at RT. We believe that this work can finally clear the doubts and concerns about the feasibility of CW RT operation of nanolasers with sub-wavelength size metallic cavities, and pave the way for eventual applications of such lasers.

Realizing sub-wavelength metallic-cavity lasers that could operate significantly above threshold under CW RT condition poses significant challenges. The large loss in metallic cavity leads to an intrinsic high threshold. The small device size requires extremely precise fabrication. Even small fabrication imperfection would mean a large relative error and thus makes the already high threshold unattainable or device could barely operation above threshold. One of the most significant fabrication challenges is to achieve near single-crystal silver quality, or realizing silver grain sizes comparable to the device sizes. Given the large surface-to-volume ratio and presence of several interfaces, it is both critically important and extremely challenging to achieve high surface quality. The optimized deposition and post annealing process eventually led to a near-single crystal silver quality with grain size comparable with the device feature size, leading to improved heat dissipation and reduced loss<sup>34</sup>. The optimized surface treatment involving a

combination of oxygen plasma and dilute phosphoric acid processing led to higher surface quality and low surface recombination. Our systematic design optimization and fabrication experiments showed the best device performance with silver thickness of 30 nm. Detailed discussions about the relationship between fabrication precision and device performance, as well as details of fabrication challenges can be found in the Supplementary Information.

Devices were mounted to a heat sink which also formed a p-contact and were forward biased by a DC voltage source. Measurement was conducted at 294 K. Emission from the backside of the substrate was collected by an objective lens and detected by a spectrometer equipped with a liquid nitrogen cooled InGaAs array detector. The light output versus current (L-I curve) for a device with optical cavity dimensions (including the SiN layer) of  $1.15 \text{ (W)} \times 1.39 \text{ (L)} \times 1.7 \text{ (H)} \mu\text{m}^3 = 0.67 \lambda^3$  ( $\lambda = 1591 \text{ nm}$ ) is shown in Fig. 2a. The L-I curve shows a clear turn-on threshold around 1.1 mA. Above the threshold, the integrated lasing mode intensity increases linearly with injection current. The integrated spontaneous emission intensity initially increases faster than the lasing mode intensity but shows a gradual clamping trend afterwards, giving way to the lasing mode. Well below threshold and close to transparency, the full width at half maximum (FWHM) of the lasing peak is 6.8 nm, corresponding to a cavity quality factor of 235. The FWHM shows a rapid decrease with increasing current and further drops to 0.5 nm at 2.02 mA. Such intensity and linewidth behavior is typical of a laser transition from below to above threshold as pumping current increases. As shown in Fig. 2b, the threshold behavior is accompanied by a significant blue shift of the laser wavelength from 1601 nm (well below threshold) to 1591 nm (above threshold) due to the band filling effect. Result from the polarization resolved measurement (Fig.

2c) shows that the far field laser emission measured directly normal to the substrate is predominantly linearly polarized along the length direction (Z direction) of the cavity.

Optical mode properties in this device were investigated through three-dimensional finite-difference time-domain (FDTD) simulations. A mode ( $E_{106}$ , corresponding to 1, 0 and 6 E-field nodes in x, y, and z direction of the cavity, see Supplementary Information) with Q-factor of 428 is identified as the lasing mode. Using the surface equivalence theorem<sup>35</sup>, the far field radiation in the direction normal to the substrate for this mode is calculated and shows linear polarization along the Z direction, which matches the polarization measurement results. The effective mode volume is estimated to be  $V_{eff}=10.29(\lambda/2n_{eff})^3$ , and the confinement factor is 0.645 (see Supplementary Information). The mode profile is shown in Fig. 3a. The Q-factor from experiment is significantly lower than in the simulation, and the difference is likely due to the imperfections of the fabrication, such as deviation of the electron beam lithography pattern from a perfect rectangle, non-vertical cavity sidewalls.

To understand the lasing behavior, rate equations are used to model a single mode nanolaser at RT (see Supplementary Information). Enhanced spontaneous emission into the lasing mode, or the Purcell effect, is taken into account by Purcell factor  $F$  which is calculated to be 13.88 using

$$F = \frac{6Q(\lambda/2n_{eff})^3}{\pi^2 V_{eff}} \quad 36.$$

Surface recombination is also considered as an essential parameter given the large surface area to volume ratio of such a sub-wavelength cavity device. Solving for the steady-state photon density and current of the rate equations, we found a good agreement between the measured and calculated L-I curves (Fig. 3b). The Purcell effect enhanced spontaneous emission factor  $\beta$  is estimated to be 0.048, which is two to three orders larger than

conventional ridge waveguide lasers<sup>37,38</sup> and one order larger than typical vertical cavity surface emitting lasers (VCSELs)<sup>39</sup>.

Plotting the L-I curve on a log-log scale, we can clearly see in Fig. 3b three regions with different slopes, representing the evolution of device output from spontaneous emission to threshold transition and eventually above-threshold lasing. Due to the change of slopes around threshold in the log-log scale L-I curve, it is interesting to plot the slope as function of pumping current. As expected, a peak is observed on such a plot (Fig. 3b, right Y axis). Since this peak represents the most dramatic transition of the laser behavior from amplified spontaneous emission to lasing, we think it is a good measure of laser threshold and can be extracted from the experimental L-I measurement directly (see Supplementary Information). Below the threshold transition region, we observed a slope of 2 in the log-log scale L-I curve. Well below threshold, the lasing mode emission is dominated by spontaneous emission and a linear scaling is expected if current is also dominated by spontaneous emission. The superlinear scaling below threshold indicates that the current contains significant contributions from non-radiative recombinations such as surface recombination and Shockley-Read-Hall (SRH) process. In such a sub-wavelength device, we estimate the surface recombination lifetime is on the order of nanoseconds. Typical bulk SRH recombination lifetime in metal organic chemical vapor deposition (MOCVD) grown high quality intrinsic III-V semiconductors is hundreds of nanoseconds<sup>40</sup>, so SRH process is negligible compared to surface recombination and therefore ignored in our rate equation analysis. A surface recombination velocity (SRV) of  $5 \times 10^4$  cm/s is obtained through rate equation fitting. This value is lower than typical SRV of InGaAs structures produced by dry etching processes which is  $1 \sim 2 \times 10^5$  cm/s<sup>40,41</sup>, and approaches the lowest value reported to our

knowledge<sup>42</sup>. At the threshold, 41.7% and 36.0% of injected carriers are consumed by surface and Auger recombinations respectively. To further investigate the influence of surface recombination, we plot the ratio of surface recombination current to threshold current as a function of SRV in Fig. 3c using the calculation results from the rate equations. When SRV increases to  $7 \times 10^4$  cm/s, surface recombination will consume more than half of the injected carriers and will significantly reduce the lifetime of the device. We believe that our new surface treatment is responsible for this low SRV. Using the same rate equation fitting, we obtain the SRV at 200K for devices with various SiN thicknesses from our previous fabrication runs and convert them to RT using  $\nu_s \propto T^{1/2}$  (Ref. 43,  $\nu_s$  is SRV,  $T$  is the ambient temperature in Kelvin). In inset of Fig. 3c, the black squares represent values of SRVs extrapolated from previous runs. Following the trends of the previous runs, the SRV should fall between the two dashed lines. But the SRV of the new devices with 30 nm SiN falls below the expected band, as indicated by the red square, indicating a significantly better surface quality. We believe that the low SRV is one of the key factors to achieve good device performance<sup>44</sup>.

In summary, by overcoming several challenges in nanoscale fabrication and by systematical design and optimization, we demonstrated record performance of RT CW operation of a semiconductor nanolaser with a sub-wavelength metallic cavity, comparable to conventional semiconductor lasers, thus achieving a long sought goal in sub-wavelength metallic cavity lasers. The linewidth is almost an order of magnitude narrower than the previously reported value<sup>26</sup>, and the Q value under lasing condition is comparable to some of the best previous RT lasing demonstrations with pulse optical pumping<sup>2, 7-8</sup>. We believe that our achievement is critical in many respects. This unambiguous demonstration proves that such sub-wavelength nanolasers



with metallic cavities are capable of RT operation with similar characteristic performance to a conventional semiconductor laser. Overcompensating metal loss at RT by semiconductor gain also has a profound impact on other active plasmonic devices and metamaterial structures, especially under CW electrical injection. Overcoming major technical challenges in the fabrication of sub-wavelength devices represents a significant advance in micro/nanofabrication. In terms of technological applications, RT CW electrical injection operation represents a key milestone for the practical implementation of such devices as one key component of future nanophotonic systems. Currently, the lifetime of our laser is still limited at RT, possibly due to degradation of the surface quality of InGaAs under the large injection current at RT. We also observed in our experiments that devices with thicker SiN layer tend to have shorter lifetimes. On the other hand, a thinner dielectric layer leads to smaller Q and higher threshold gain. Thus, the thickness of the dielectric layer should be optimized with the above trade-off carefully considered. Improved processing techniques for better surface passivation or new device designs, for example using quantum wells as the active medium to lower the threshold current, are possible solutions to relieve the conflict as well. We believe that, with further advances in processing techniques and device designs, fully developed metallic nanolasers suitable for practical applications will be realized in the near future, thus opening new vistas for nanophotonic applications.

## **METHODS SUMMARY**

### **Device fabrication**

The device pattern was defined by electron beam lithography on a MOCVD grown wafer. The InP/InGaAs/InP pillar was formed by inductively coupled plasma etching. SiN layer was deposited by plasma enhanced chemical vapor deposition to cover all sides of the pillar. Planarization and reactive ion etching were conducted to remove the SiN layer on top of the pillar, thus forming the n contact via electron beam evaporation afterwards. The whole structure was then encapsulated in silver. The p contact was formed on the heavily doped InGaAsP layer underneath the pillar, thus enabling electrical injection. We optimized silver deposition rate (at 4 nm/s), deposition thickness (to 1  $\mu\text{m}$ ) and annealing process to improve silver quality and its grain size. The silver grain size we obtained is up to 1  $\mu\text{m}$ . For devices with dimensions around 1  $\mu\text{m}$ , such silver layer almost behaves as a single crystal, which leads to the significant devices performances. Detailed description of device fabrication can be found elsewhere<sup>26</sup>.

### **Optical Measurement**

The fabricated device was forward biased by a DC voltage source and measured at RT of 294K. The laser emission from the backside of substrate was collected by a 15x objective and directed to an optical spectrometer equipped with a liquid nitrogen cooled InGaAs array detector. For emission intensity measurement, coarse grating with 1 nm resolution was used. For measurement related to linewidth, peak position, fine grating was chosen to obtain 0.2 nm resolution. A Glan-Taylor polarizing prism was used for polarization measurement.

## References

1. Oulton, R. F. *et al.* Plasmon lasers at deep subwavelength scale. *Nature* **461**, 629-632 (2009).
2. Noginov, M. A. *et al.* Demonstration of a spaser-based nanolaser. *Nature* **460**, 1110-1112 (2009).
3. Khajavikhan, M. *et al.* Thresholdless nanoscale coaxial lasers. *Nature* **482**, 204-207 (2012).
4. Ning, C. Z. Semiconductor nanolasers. *Phys. Stat. Sol. B* **247**, 774-788 (2010).
5. Bergman, D. J. & Stockman, M. I. Surface plasmon amplification by stimulated emission of radiation: quantum generation of coherent surface plasmon in nanosystems. *Phys. Rev. Lett.* **90**, 027402-027405 (2003).
6. Hill, M. T. *et al.* Lasing in metallic-coated nanocavities. *Nat. Photonics* **1**, 589-594 (2007).
7. Nezhad, M. P. *et al.* Room-temperature subwavelength metallo-dielectric lasers. *Nat. Photonics* **4**, 395-399 (2010).
8. Ma, R. M., Oulton, R. F., Sorger, V. J., Bartal, G. & Zhang, X., Room-temperature sub-diffraction-limited plasmon laser by total internal reflection. *Nat. Mater.* **10**, 110-113 (2011).
9. For convenience, the wavelength here refers to wavelength in vacuum.
10. Tandaechanurat, A. *et al.* Lasing oscillation in a three-dimensional photonic crystal nanocavity with a complete bandgap. *Nat. Photonics* **5**, 91-94 (2011).
11. Ellis, B. *et al.* Ultralow-threshold electrically pumped quantum-dot photonic-crystal nanocavity laser. *Nat. Photonics* **5**, 297-300 (2011).
12. Matsuo, S. *et al.* High-speed ultracompact buried heterostructure photonic-crystal laser with 13 fJ of energy consumed per bit transmitted. *Nat. Photonics* **4**, 648-654 (2010).

13. Matsuo, S. *et al.* Room-temperature continuous-wave operation of lateral current injection wavelength-scale embedded active-region photonic-crystal laser. *Opt. Express* **20**, 3773-3780 (2012).
14. Maslov, A. V. & Ning, C. Z. Size reduction of a semiconductor nanowire laser using metal coating. *SPIE Proceed* **6468**, 646801-646807 (2007).
15. Hill, M. T. *et al.* Lasing in metal-insulator-metal sub-wavelength plasmonic waveguides. *Opt. Express* **17**, 11107-11112 (2009).
16. Ding, K. *et al.* Electrical injection, continuous wave operation of subwavelength-metallic-cavity lasers at 260K. *Appl. Phys. Lett.* **98**, 231108-231110 (2011).
17. Lee, J. H. *et al.* Electrically pumped sub-wavelength metallo-dielectric pedestal pillar lasers. *Opt. Express* **19**, 21524-21531 (2011).
18. Perahia, R., Alegre, T. P. M., Safavi-Naeini, A. H. & Painter, O. Surface-plasmon mode hybridization in subwavelength microdisk lasers. *Appl. Phys. Lett.* **95**, 201114-201116 (2009).
19. Yu, K., Lakhani, A. M. & Wu, M. C. Subwavelength metal-optic semiconductor nanopatch lasers. *Opt. Express* **18**, 8790-8799 (2010).
20. Lakhani, A. M., Kim, M., Lau, E. K. & Wu, M. C. Plasmonic crystal defect nanolaser. *Opt. Express* **19**, 18237-18245 (2011).
21. Kwon, S. H. *et al.* Subwavelength plasmonic lasing from a semiconductor nanodisk with silver nanopan cavity. *Nano. Lett.* **10**, 3679-3683 (2010).
22. Lu, C. Y., Chang, S. W., Chuang, S. L., Germann, T. D. & Bimberg, D. Metal-cavity surface-emitting microlaser at room temperature. *Appl. Phys. Lett.* **96**, 251101-251103 (2010).

23. Marell, M. J. H. *et al.* Plasmonic distributed feedback lasers at telecommunications wavelengths. *Opt. Express* **19**, 15109-15118 (2011).
24. Zhang, Z. *et al.* Visible submicron microdisk lasers. *Appl. Phys. Lett.* **90**, 111119-111121 (2007).
25. Liu, Z. *et al.* Continuous-wave subwavelength microdisk lasers at  $\lambda = 1.53 \mu\text{m}$ . *Opt. Express* **18**, 19242-19248 (2010).
26. Ding, K. *et al.* Room-temperature continuous wave lasing in deep-subwavelength metallic cavities under electrical injection. *Phys. Rev. B* **85**, 041301-041305 (2012).
27. Ding, K. *et al.* Room temperature CW operation of metal-semiconductor plasmonic nanolasers with subwavelength cavity. Conference on Lasers and Electro-Optics, Baltimore, MD, May 2011.
28. Kita, S., Nozaki, K. & Baba, T. Refractive index sensing utilizing a cw photonic crystal nanolaser and its array configuration. *Opt. Express* **16**, 8174-8180 (2008).
29. Palais, J. C. *Fiber Optic Communications* Ch. 12 (Prentice Hall, Englewood Cliffs NJ, 1988).
30. The main results of this paper were reported by Ding, K. *et al.* Record performance of a CW metallic subwavelength-cavity laser at room temperature. Conference on Lasers and Electro-Optics, San Jose, CA, May 2012.
31. Coleman, J. J., Bryce, A. C. & Jagadish, C. (ed.), *Advances in Semiconductor Lasers* (Academic Press, San Diego CA, 2012), pp. 459-463.
32. Min, B. *et al.* Erbium-implanted high-Q silica toroidal microcavity laser on a silicon chip. *Phys. Rev. A* **70**, 033803-033812 (2004).

33. Gong, Y. *et al.* Linewidth narrowing and Purcell enhancement in photonics crystal cavities on an Er-doped silicon nitride platform. *Opt. Express* **18**, 2601-2612 (2010).
34. Kuttge, M. *et al.* Loss mechanisms of surface plasmon polaritons on gold probed by cathodoluminescence imaging spectroscopy. *Appl. Phys. Lett.* **93**, 113110-113112 (2008).
35. Balanis, C. A. *Advanced Engineering Electromagnetics* (Wiley, New York, 1989), pp. 329-334.
36. Robinson, J. T., Manolatou, C., Chen, L. & Lipson, M. Ultrasmall mode volumes in dielectric optical microcavities. *Phys. Rev. Lett.* **95**, 143901-143904 (2005).
37. Petermann, K. Calculated spontaneous emission factor for double-heterostructure injection lasers with gain-induced waveguiding. *IEEE J. Quantum Electron.* **15**, 566-570 (1979).
38. Goodwin, J. C. & Garside, B. K. Measurement of spontaneous emission factor for injection lasers. *IEEE J. Quantum Electron.* **18**, 1264-1271 (1982).
39. Shin, J. H., Ju, Y. G., Shin, H. E. & Lee, Y. H. Spontaneous emission of oxidized vertical-cavity surface-emitting lasers from the measured below-threshold cavity loss. *Appl. Phys. Lett.* **70**, 2344-2346 (1997).
40. Beister, G. & Wenzel, H. Comparison of surface and bulk contributions to non-radiative currents in InGaAs/AlGaAs laser diodes. *Semicond. Sci. Technol.* **19**, 494-500 (2004).
41. Hu, S. Y. *et al.* Lateral carrier diffusion and surface recombination in InGaAs/AlGaAs quantum-well ridge-waveguide lasers. *J. Appl. Phys.* **76**, 4479-4487 (1994).
42. Boroditsky, M. *et al.* Surface recombination measurements on III-V candidate materials for nanostructure light-emitting diodes. *J. Appl. Phys.* **87**, 3497-3504 (2000).
43. Forchel, A. *et al.* Transport and optical properties of semiconductor quantum wires. *J. Vac. Sci. Technol. B* **9**, 444-450 (1991).

44. Chen, R. *et al.* Nanolasers grown on silicon. *Nat. Photonics* **5**, 170-175 (2010).

**Acknowledgment** This research is supported by the Defense Advanced Research Project Agency (W911NF-07-1-0314) and Air Force Office for Scientific Research (AFOSR, FA9550-10-01-0444). We would like to thank D. Sahin, B. Smalbrugge, E. J. Geluk, T. D. Vries, and J. Bolk for their technical assistance in the cleanroom fabrication, and M. Smit for his generosity in hosting one of the authors (K. D.) at COBRA Institute during his visit.

**Author Contributions** K. D. performed nanolaser design, simulation, fabrication, characterization and manuscript preparation. C. Z. N. initiated the current research, supervised the overall research project, and involved in the data analysis and manuscript preparation. M. T. H. also contributed to process development, device design and fabrication as well. Z. C. L. and L. J. Y. contributed to device characterization. P. J. v. V. was responsible for the MOCVD epitaxial growth.

**Author Information** Reprints and permissions information is available at [www.nature.com](http://www.nature.com). The authors declare no competing financial interests. Correspondence and requests for material should be addressed to C. Z. N. ([cning@asu.edu](mailto:cning@asu.edu)).

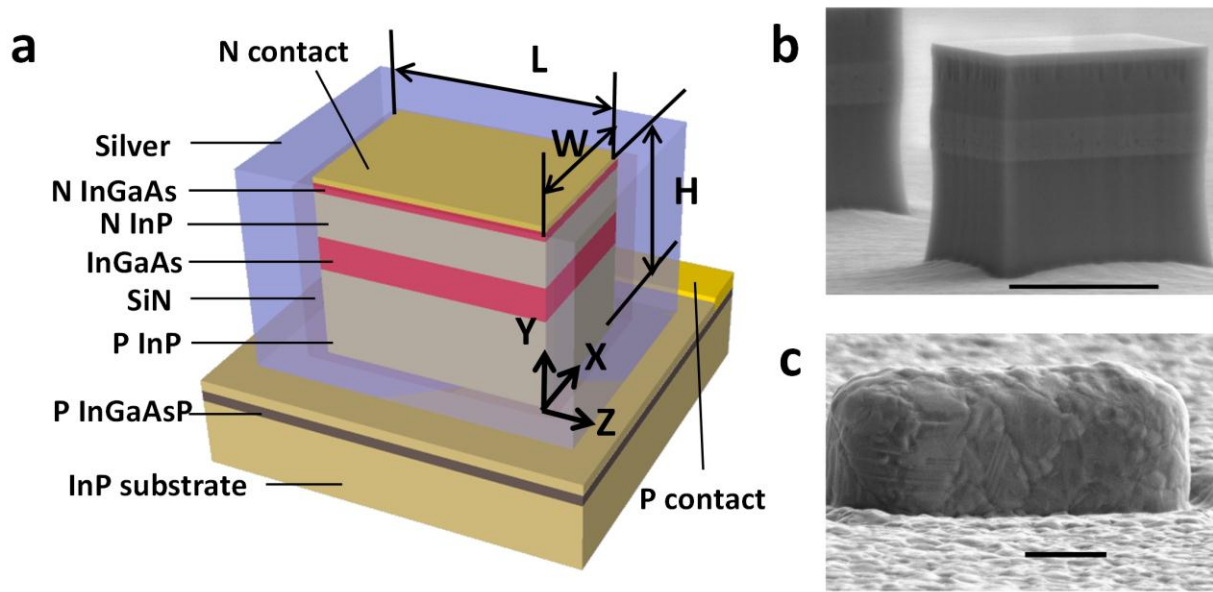


**Figure 1| Structure of the metallic-cavity semiconductor nanolaser. a.** Semiconductor pillar with a rectangular cross section is encapsulated in silver to form a metallic cavity. **b.** Scanning electron microscope (SEM) image of the semiconductor core of the laser structure. **c.** SEM image of metallic cavity after coating the semiconductor/SiN core with silver. Large crystalline grain size up to 1 μm is obtained. Scale bars in (b) and (c) are both 1 μm.



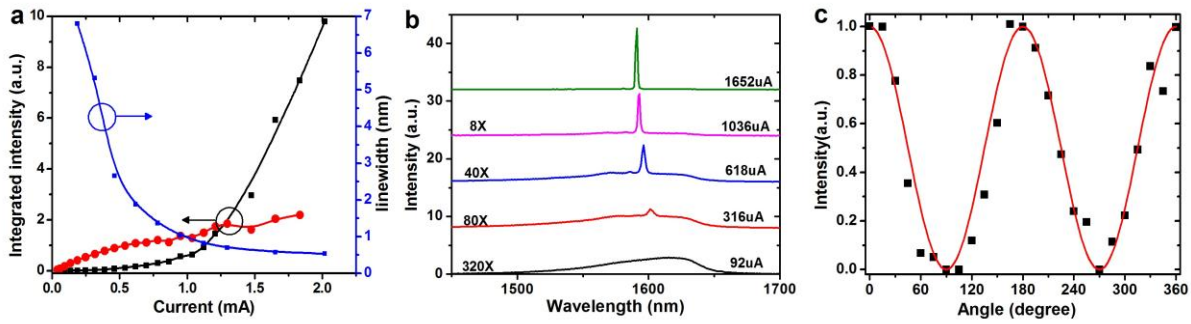


**Figure 2| CW Laser characteristics at room temperature. a.** L-I and FWHM-I curve at 294K under DC current injection of the laser. ■: integrated lasing mode intensity; ●: integrated spontaneous emission intensity. **b.** Spectra (offset for clarity) of this device at different currents. **c.** Polarization resolved measurement result, where Z-direction corresponds to 0 and 180 degrees.

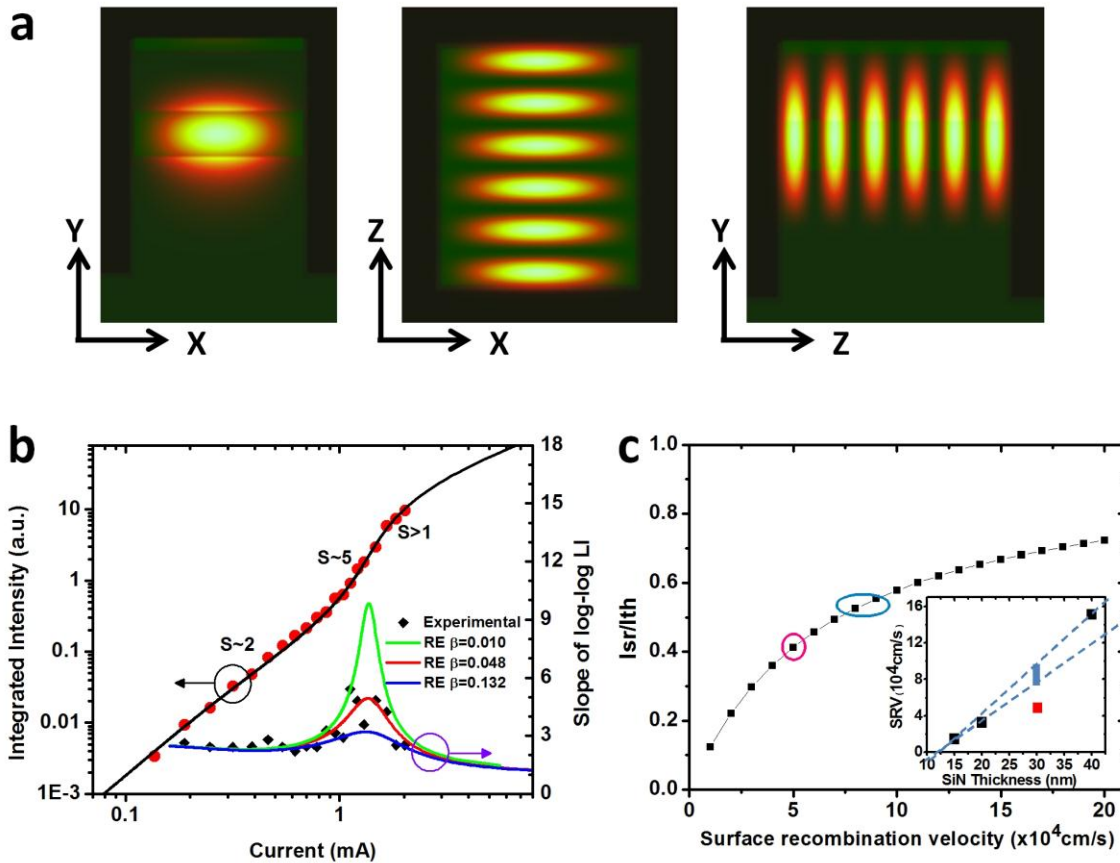


**Figure 3| Modal properties and threshold behavior for the metallic-cavity semiconductor nanolaser. a.**  $|E|^2$  patterns of  $E_{106}$  mode. **b.** L-I curve plotted on a log-log scale and its slope from experimental result (red solid circle  $\bullet$  and black diamond  $\blacklozenge$ ) and from rate equation (RE) calculation (solid line), with slopes given for three regions. Slopes from RE with  $\beta=0.01$  and  $0.132$  are plotted for comparison. **c.** Ratio of  $I_{sr}$ : surface recombination current versus  $I_{th}$ : threshold current as a function of SRV. Inset: SRVs extracted from rate equations for devices with different SiN thicknesses. The three black squares represent SRV values extracted from previous runs and the red square is from the new device. Blue bar is the expectation of surface recombination for 30 nm SiN following the trend of the three black squares.  $I_{sr}/I_{th}$  values for real experiment SRV and expected SRV are marked in red and blue circles respectively.